



HAL
open science

Determination of absolute Np L X-ray emission intensities from ^{241}Am decay using a metallic magnetic calorimeter

Matias Rodrigues, Martin Loidl, Sylvie Pierre

► **To cite this version:**

Matias Rodrigues, Martin Loidl, Sylvie Pierre. Determination of absolute Np L X-ray emission intensities from ^{241}Am decay using a metallic magnetic calorimeter. *Metrologia*, 2023, 60, pp.025005. 10.1088/1681-7575/acb99f. cea-04080914

HAL Id: cea-04080914

<https://cea.hal.science/cea-04080914>

Submitted on 25 Apr 2023

HAL is a multi-disciplinary open access archive for the deposit and dissemination of scientific research documents, whether they are published or not. The documents may come from teaching and research institutions in France or abroad, or from public or private research centers.

L'archive ouverte pluridisciplinaire **HAL**, est destinée au dépôt et à la diffusion de documents scientifiques de niveau recherche, publiés ou non, émanant des établissements d'enseignement et de recherche français ou étrangers, des laboratoires publics ou privés.



ACCEPTED MANUSCRIPT

Determination of absolute Np L X-ray emission intensities from Am-241 decay using a metallic magnetic calorimeter

To cite this article before publication: Matias Rodrigues *et al* 2023 *Metrologia* in press <https://doi.org/10.1088/1681-7575/acb99f>

Manuscript version: Accepted Manuscript

Accepted Manuscript is “the version of the article accepted for publication including all changes made as a result of the peer review process, and which may also include the addition to the article by IOP Publishing of a header, an article ID, a cover sheet and/or an ‘Accepted Manuscript’ watermark, but excluding any other editing, typesetting or other changes made by IOP Publishing and/or its licensors”

This Accepted Manuscript is © 2023 BIPM & IOP Publishing Ltd.

During the embargo period (the 12 month period from the publication of the Version of Record of this article), the Accepted Manuscript is fully protected by copyright and cannot be reused or reposted elsewhere.

As the Version of Record of this article is going to be / has been published on a subscription basis, this Accepted Manuscript is available for reuse under a CC BY-NC-ND 3.0 licence after the 12 month embargo period.

After the embargo period, everyone is permitted to use copy and redistribute this article for non-commercial purposes only, provided that they adhere to all the terms of the licence <https://creativecommons.org/licenses/by-nc-nd/3.0>

Although reasonable endeavours have been taken to obtain all necessary permissions from third parties to include their copyrighted content within this article, their full citation and copyright line may not be present in this Accepted Manuscript version. Before using any content from this article, please refer to the Version of Record on IOPscience once published for full citation and copyright details, as permissions will likely be required. All third party content is fully copyright protected, unless specifically stated otherwise in the figure caption in the Version of Record.

View the [article online](#) for updates and enhancements.

Determination of absolute Np L X-ray emission intensities from Am-241 decay using a metallic magnetic calorimeter

Matias Rodrigues¹, Martin Loidl¹ and Sylvie Pierre¹

¹ Université Paris-Saclay, CEA, List, Laboratoire National Henri Becquerel (LNE-LNHB), F-91120 Palaiseau, France

E-mail: matias.rodrigues@cea.fr

Received xxxxxx

Accepted for publication xxxxxx

Published xxxxxx

Abstract

Photon emission intensities of radionuclides, i.e. the number of emitted photons per decay, are the single most important decay data when the photon spectrometry technique is employed in ionizing radiation metrology. However, their precise measurement is problematic because they are usually determined by photon spectrometry with spectrometers having a detection efficiency calibrated with X-ray and γ -ray emission intensities from other radionuclides. Therefore, these intensities are ultimately interdependent and correlated to some extent. A novel method was applied to determine the photon intensities of α -emitting radionuclides by measuring the ratio between the rate of photons in the full energy peaks and the rate of detected α -particles with the same detection set-up. Thus, there is no need to calibrate the detection efficiency and to standardize calibration sources by primary methods. The main condition to reach low uncertainties is to have a spectrometer with an intrinsic detection efficiency close to unity for the measured photons and α -particles. This condition was fulfilled by a metallic magnetic calorimeter (MMC) with an intrinsic efficiency of around 99% between 5 and 25 keV. In addition, the MMC provides an ultra-high energy resolution of 28 eV (full width at half maximum), facilitating the processing of the spectrum. The method was applied to determine L X-ray emission intensities from the decay of $^{241}\text{Am}(\alpha) \rightarrow ^{237}\text{Np}$ emitted between 11.9 keV and 22.4 keV. A total L X-ray emission intensity of 37.90 (12) per 100 disintegrations was obtained; the value agrees well with previous measurements and has a lower uncertainty. The uncertainties of the L X-ray groups $L\alpha$, $L\eta\beta$ and $L\gamma$ were improved by a factor of two. Moreover, due to the high-energy resolution of 28 eV, a detailed set of 33 L X-ray emission intensities are provided.

Keywords: Photon emission intensity, radionuclide metrology, metallic magnetic calorimeter

1. Introduction

During the decay of a radionuclide, the atom or the nucleus of the daughter is excited, leading to the emission of X-rays or γ -rays with characteristic energies E and photon emission intensities $I(E)$ (PEI). The PEIs are expressed as the number of photons emitted per decay. It is the most important decay parameter for quantitative analysis of a radioactive material by means of photon spectrometry [1]. Indeed, in ionizing radiation metrology, the activity A of a radionuclide in a source at the measurement date t is determined from the energy spectrum obtained with an energy dispersive spectrometer. In stationary conditions, i.e. when the measurement live time Δt is much smaller than the radionuclide half-life, the activity is given by the equation (1):

$$A(t) = \frac{N_{FEP}(E)}{I(E) \cdot \varepsilon_{FEP}(E) \cdot \Delta t} = \frac{n_{FEP}(E)}{I(E) \cdot \varepsilon_{FEP}} \quad (1)$$

where $N_{FEP}(E)$ and $n_{FEP}(E)$ are respectively the number of counts and the count rate in the full-energy peak (FEP) at the characteristic energy E , ε_{FEP} is the FEP detection efficiency, i.e. the probability for a photon emitted by the source to deposit all of its energy in the detector.

The FEP detection efficiency is usually obtained using standard radioactive sources with calibrated activity and well-known PEIs in the appropriate energy range [2,3] and following:

$$\varepsilon_{FEP}(E) = \frac{N_{FEP}(E)}{I(E) \cdot A(t) \cdot \Delta t} = \frac{n_{FEP}(E)}{I(E) \cdot A(t)} \quad (2)$$

Therefore, the activity measurement of a radionuclide by photon spectrometry is a relative method that strongly relies on the PEIs from other radionuclides, both to quantify the radionuclides in activity (equation (1)) and to establish the detection efficiency curves (equation (2)). In addition, the uncertainty of the PEIs is one of the major contributions to the uncertainty budget of the activity measured with photon spectrometry. At best, their relative uncertainties are about 0.5%, but generally 1-2%, in particular in the problematic low energy range below 100 keV [2,4,5].

PEIs of a radionuclide are measured by semiconductor spectrometers generally with the same methodology as for the activity measurement (equation (1)), in this case using:

$$I(E) = \frac{N_{FEP}(E)}{A(t) \cdot \varepsilon_{FEP}(E) \cdot \Delta t} = \frac{n_{FEP}(E)}{A(t) \cdot I(E) \cdot \varepsilon_{FEP}(E)} \quad (3)$$

i.e. they are determined by measuring the photon energy spectrum of a source with a precisely determined activity A and with a spectrometer with a well-established detection efficiency curve.

Therefore, the need to decrease the uncertainty of PEIs is part of a vicious circle; it requires a detection efficiency with a lower uncertainty, itself limited by PEIs from radionuclides.

Several studies have proposed to determine PEIs by a spectrometer with an efficiency established independently of the PEIs. The FEP detection efficiency, ε_{FEP} , can be expressed as the product of the geometry factor f_{geo} and the intrinsic detector efficiency ε_{int} . The factor, f_{geo} , refers to the probability that an emitted photon to go in the direction of the detector (or the collimator aperture) and the efficiency ε_{int} refers to the probability that a photon in the direction of the detector will deposit all its energy in the detector. A third factor, t_{win} , can be introduced, related to the probability the photons will be transmitted through the windows between the source and the detector (vacuum or entrance window). The factor f_{geo} can be accurately calculated by measuring precisely the dimensions of the detection geometry (source and collimator diameters, and source-collimator distance) as it is the case for defined solid angle (DSA) α -particle counting [6,7]. Bambynek proposed to apply the DSA technique for the measurement of activity by photon counting [8]. Later, DSA photon spectrometry with proportional counters or scintillators was developed for measuring emission intensities of radionuclides [9,10]. The advantage of these detectors is their well-defined and simple detection geometry to determine the geometrical efficiency, f_{geo} , associated with an intrinsic efficiency close to 100% that helps to minimize its correction. However, they have a poor energy resolution for spectrometry; proportional counters have an intrinsic efficiency of 100% only achievable below about 10 keV, hence, measurements of emission intensities did not reach accuracies better than 1% below 10 keV [7], and scintillators were applied to some specific cases [9].

DSA photon spectrometry was then studied by Martin and Burns to measure PEIs with a HPGe spectrometer independently of other radionuclides [11]. In this case, the intrinsic efficiency has to be calculated analytically using atomic fundamental parameters or more frequently numerically with Monte Carlo (MC) simulations of particle transport through matter. Nevertheless, the intrinsic efficiency ε_{int} of semiconductor spectrometers is difficult to calculate accurately due to the contributions of many energy-dependent interacting processes:

- the transmission of photons through the detector absorber and the escape of secondary particles,
- the incomplete collection of electron-hole pairs in the dead layers,
- scattering photons around the detector environment overlapping with the FEPs [12,13].

In addition, when MC simulations are performed, a precise knowledge of the dimensions of the detector is needed which is not guaranteed by the manufacturers and difficult to access. Consequently, the critical dimensions, in particular the dead

layers [14,15], have to be fitted to find the best agreement between simulations and experimental data from standard sources, and ultimately these methods rely on PEIs [16,17]. Instead of calculating the intrinsic efficiency, Lépy and co-workers precisely characterized it for one of their semiconductor spectrometers with a monochromatic photon source; in addition, the geometrical efficiency was calibrated by a ^{55}Fe source with a calibrated emission rate [18]. They were able to measure the total L X-ray emission intensities from the decay of ^{241}Am independently of other radionuclide PEIs with a relative uncertainty of 0.7%.

In the present work, we propose a new method for measuring the photon emission intensities of 100% α -emitting radionuclides independently of any efficiency calibration based on PEIs, and without the need to measure a source with a calibrated activity. In a simplified way, the method consists in measuring, with the same detection set-up, the ratio between the photon rate and the α -particle rate from the source; the photon intensity $I(E)$ emitted at energy E is a given by:

$$I(E) = \frac{n_{FEP}(E) \cdot \varepsilon_{\alpha}}{n_{\alpha} \cdot \varepsilon_{FEP}(E)} \quad (4)$$

where n_{FEP} and n_{α} are respectively the count rates of detected photons in the full energy peaks and detected α -particles, each rate $n = N/\Delta t$, where N is the number of counts and Δt is the measurement live time.

ε_{FEP} and ε_{α} are respectively the detection efficiencies for the photons of energy E and the α -particles.

For radionuclides decaying only by α -particle emission, this method can be very precise without any calibration on the condition that $\varepsilon_{FEP} \approx \varepsilon_{\alpha} \approx f_{geo}$; which means that the detector must be able to measure both α -particles and photons, with the same geometrical efficiency and with intrinsic efficiencies for photons and α -particles as close as possible to unity. For α -particles, since their energy is absorbed in a few μm , an intrinsic efficiency close to 100% is readily achieved.

The LNE-LNHB has developed a detection set-up for photon spectrometry called SMX3 that fulfills these requirements. SMX3 is a metallic magnetic calorimeter (MMC) with a special absorber conceived to provide an intrinsic efficiency of 99% between 5 keV and 25 keV [19]. Although it is not optimized for this purpose, it is able to measure α -particles with the same detection geometry only by removing a beryllium window that stops α -particles for most other measurements. Moreover, MMCs are a type of thermal cryogenic detector with the main advantage of having an excellent energy resolution, about one order of magnitude better than semiconductor detectors [20].

The method was applied to the measurement of the L-X ray emission intensities from ^{241}Am α -decay. Americium-241 was

chosen because it is one of the best known α -emitting radionuclides, commonly used as a calibration source below 100 keV in the metrology of ionizing radiation and in many other applications [2]. On the one hand, this allows the present results to be compared with the most precise measurements of PEIs below 100 keV [21], and on the other hand, this allows disseminating accurate and reliable PEIs to end users for the efficiency calibration of their spectrometers with ^{241}Am sources. Furthermore, the resolution of SMX3 is a very important asset in this case because it can separate the tens of X-ray lines, and provide as many PEIs, which is not possible with semiconductor detectors.

2. The experimental detection set-up

2.1 General principle of MMCs

MMCs are thermal cryogenic detectors, i.e. the absorbed energy E from an incoming particle is measured as a temperature rise:

$$\Delta T = \frac{E}{C} \quad (5)$$

where C is the detector heat capacity.

An MMC detector for photon spectrometry is often composed of a metallic absorber where the particle interacts and deposits partially or fully its energy, leading to a temperature elevation ΔT . The absorber is tightly thermally coupled to a paramagnetic sensor made of gold (or silver) doped with a few hundred ppm of Er [20]. The sensor is magnetized by a magnetic field of a few mT, and acts as a thermometer by converting the change of temperature in a variation of magnetization. The latter can be precisely measured by a DC SQUID sensor. The paramagnetic sensor is weakly thermally coupled to a heat bath, at a temperature T_0 , through a weak thermal link with a thermal conductance G . Therefore, each deposit of energy E in the detector is measured as a pulse with a height proportional to E and with a decay time constant ($1/e$) of $\tau_d = C/G$. The energy resolution of MMCs is not limited by the statistical uncertainty on the number of excited states created by the absorbed energy, as it is the case e.g. for the creation of electron-hole pairs in a semiconductor. For thermal cryogenic detectors, the energy resolution is given by the signal-to-noise ratio. The intrinsic noise limit is set by the so-called thermodynamic fluctuation noise (TFN), i.e. the statistical fluctuations of the detector internal energy with the thermal bath through the weak thermal link; the TFN causes a standard deviation on the energy resolution of:

$$\sigma_{E_{TFN}} = \sqrt{4 \cdot k_B \cdot T_0 \cdot C^2} \quad (6)$$

where k_B is the Boltzmann constant.

Knowing that the heat capacity of non-superconducting metal absorbers decreases proportionally with the temperature, and considering equations (5) and (6): both the signal amplitude increases and the noise decreases toward very low temperature. Around 20 mK, very high-energy resolutions are achieved, up to more than one order of magnitude better than semiconductor spectrometers [22,23].

2.2 The dedicated MMC SMX3

In this work, the SMX3 MMC detector was used (figure 1). It was specially conceived for photon spectrometry below 25 keV, it has [19]:

- a confirmed full width at half maximum (FWHM) energy resolution of about 30 eV up to 166 keV,
- an intrinsic detection efficiency of about 99% between 5 and 25 keV,
- an maximum acceptable count rate up to about 10 s^{-1} ,
- a total absorber area of 4 mm^2 .

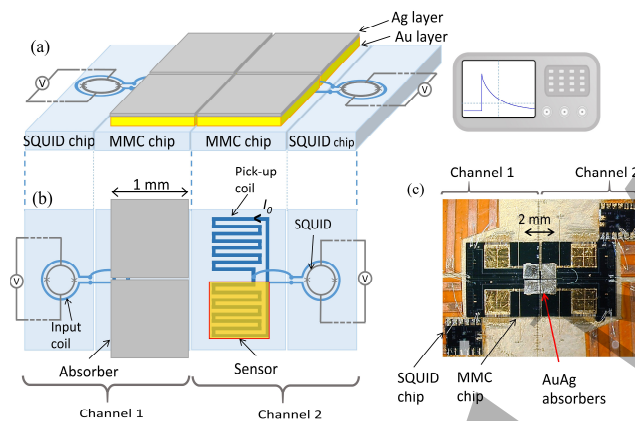


Figure 1. a) and b) Schemes of the MMC SMX3 with its four pixel absorbers and its read-out by two SQUID channels. c) Photograph of the MMC and the SQUID chips (b)¹.

The SMX3 absorber is divided into 4 pixels of 1 mm^2 each. By sharing the total absorber heat capacity between pixels, the signal-to-noise ratio and the energy resolution are improved. Each absorber is attached to a magnetic Au:Er sensor with about 300 ppm of erbium and each sensor is read by a meander shaped superconducting pick-up coil [24]. Two pick-up coils are connected in parallel with a DC SQUID input coil thereby forming a superconducting magnetic flux transformer; the pulses of the two different sensors of one MMC chip cause signals with opposite polarities in the SQUID. Two SQUID channels allow reading the four pixels (figure 1). The weak

magnetic field of a few mT, required to magnetize the sensor, is created by a permanent current I_0 circulating in double meander pick-up coils.

The absorbers of SMX3 are composed of a Au-Ag bi-layer in order to achieve an intrinsic efficiency as close as possible to unity below 25 keV. Indeed, the efficiency of a single gold layer absorber calculated by MC simulations, with the code PENELOPE [25], shows a curve with three discontinuities around 13 keV (figure 2). These discontinuities are difficult to characterize. They are, firstly, due to the discontinuities of the photoelectric cross section of gold at the L_3 , L_2 and L_1 sub-shell binding energies, respectively 11.9 keV, 13.7 keV and, 14.4 keV, and secondly due to the escape of photons from the absorber surface facing the source. For the latter reason, the discontinuities are present regardless of the thickness of the absorber. Therefore, an additional layer of silver was added on top of the gold layer to reabsorb the escape photons, thus forming a Au-Ag bi-layer absorber. MC simulations have shown that it is possible to reach an efficiency close to 100% below 25 keV with thicknesses of at least $54 \mu\text{m}$ of gold and $16 \mu\text{m}$ of silver (figure 2) [19,26].

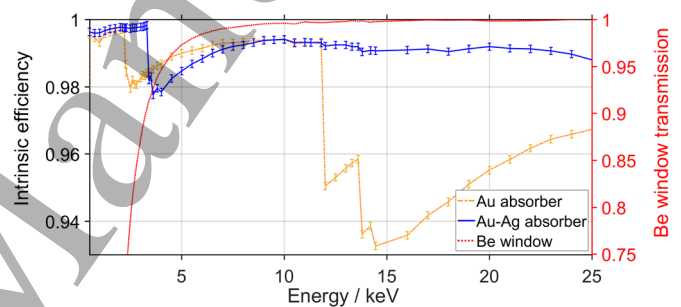


Figure 2. Left axis: intrinsic efficiencies calculated by the MC simulations, for a $70 \mu\text{m}$ thick gold absorber and for a Au-Ag absorber with $54 \mu\text{m}$ thick gold and $16 \mu\text{m}$ thick silver. Right axis: transmission of photon through the $37 \mu\text{m}$ thick beryllium window calculated by MC simulations.

The intrinsic efficiency of the bi-layer has a small discontinuity at 3.4 keV and a large discontinuity at 25.5 keV (not shown), they correspond respectively to the L_1 - and K-binding energies of silver. In the Np L-X ray energy range between 11.8 keV and 22.4 keV², the mean intrinsic efficiency is 99.03% and varies by less than 0.59%. In comparison the detection efficiencies of Si(Li) and HPGe detectors vary by more than 10% [18]. The absorbers were fabricated with the minimum required thicknesses of $54 \mu\text{m}$ of gold and $16 \mu\text{m}$ of silver in order to minimize their heat capacity and maximize the signal-to-noise ratio.

Figure 3 shows the overall detection assembly comprising: the SQUID (not shown) and the MMC chips, the source, the

¹ MMC chips were optimized, designed and produced by C. Enss' group at Kirchhoff-Institute for Physics, Heidelberg University [22].

² The $L_1 - L_3$ transition at 4.82 keV is not considered in the energy range between 11.8 keV and 22.4 keV.

tungsten collimator and the beryllium window. The latter is necessary to absorb the α -particles and the electrons emitted during the ^{241}Am decay when measuring the photon spectrum only. Indeed, the 5.5 MeV α -particles could saturate the signal output and make the SQUID electronics unstable, while the Auger and internal conversion electrons will unnecessarily pollute the spectrum and increase the dead time of the measurement. The dimensions of the detection geometry are detailed in section 3.3.

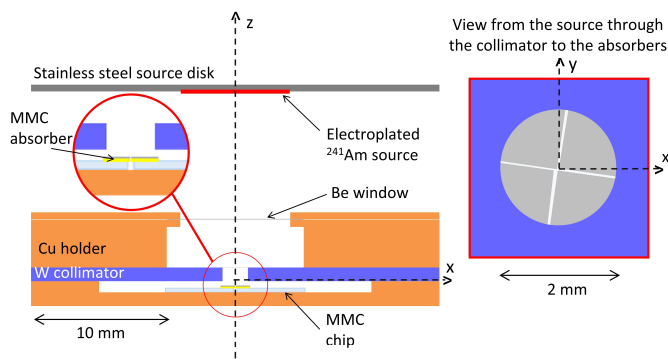


Figure 3. Left, a cross-sectional view of the experimental set-up at scale. Right, view of the square absorbers through the collimator. All parts are cylindrically symmetrical along the z -axis, except for the absorbers and chips.

3. The ^{241}Am sources

3.1 The need for two sources

Americium-241 has a half-life of 432.6 (6) a and decays by α -particle emission to ^{237}Np , the latter having a half-life of $2.144 (7) \times 10^6$ a. There are two main α -particle energies that subsequently populate the 59.54 keV and the 102.959 keV levels with a probability of 13.23% and 84.45% respectively. Among the γ -transitions, four of these are below 60 keV: 26.34 keV, 33.20 keV, 43.42 keV and 59.54 keV. They are intense and strongly converted and are responsible for 98% of the emitted L X-rays by the ^{237}Np daughter. The recommended value of the total L-X-ray emission intensity is 37.66 (17) per 100 decays [21].

Ideally the count rates n_{FEP} and n_{α} should be obtained from one spectrum, i.e. from one measurement with the same source, in order to consider the same live time, the same activity and the same source geometry (equation (4)). However, in practice, measuring both the X-rays and the α -particles at the same time would be very penalizing for the X-ray spectrum measurement. Firstly, it is not possible to achieve the best energy resolution in the photon spectrum whilst also measuring the α -particles. Indeed, with the optimal operating conditions for X-ray spectrometry, the SMX3 detector is too sensitive to measure the energies of α -particles: an α -particle of 5.5 MeV will produce a pulse of about $18 \Phi_0$ in the SQUID³ with a permanent current of $I_0 = 70$ mA in the meander pick-up coil and at a temperature of 14 mK. Such a pulse is impossible to measure without signal instabilities given the rise time of a few μs and a slew rate of the SQUID electronics of about $1 \Phi_0/\mu\text{s}$. Therefore, to measure α -particles, the detector sensitivity has to be reduced, by reducing the sensor magnetization using a smaller permanent current, thus degrading the energy resolution.

Table 1. Characteristics of the two measured ^{241}Am sources.

Source for:	Activity / Bq	Measurement date	Distance $Z_{\text{so-col}}$ / mm	Active diameter / mm
α -particles	1816.4 (11)	14/01/2022	15.845 (12)	10.5
X-rays	32169 (34)	08/05/2021	16.339 (8)	6.5

In addition, the measurement of the count rate n_{α} must be performed without any window between the source and the absorbers, meaning that all the emitted particles (α -particles, nuclear recoils, Auger and internal conversion electrons, X and γ -ray photons) emitted during the decay are detectable. As there are ten times as many emitted particles per decay as there are X-rays, most of the counting statistics would be useless, interfering in the X-ray region of interest. This is all the more penalizing since the maximum acceptable count rate of SMX3 is about 10 s^{-1} .

³ Φ_0 is the magnetic flux quantum, $1 \Phi_0 \approx 2.067833848 \times 10^{-15} \text{ Wb}$

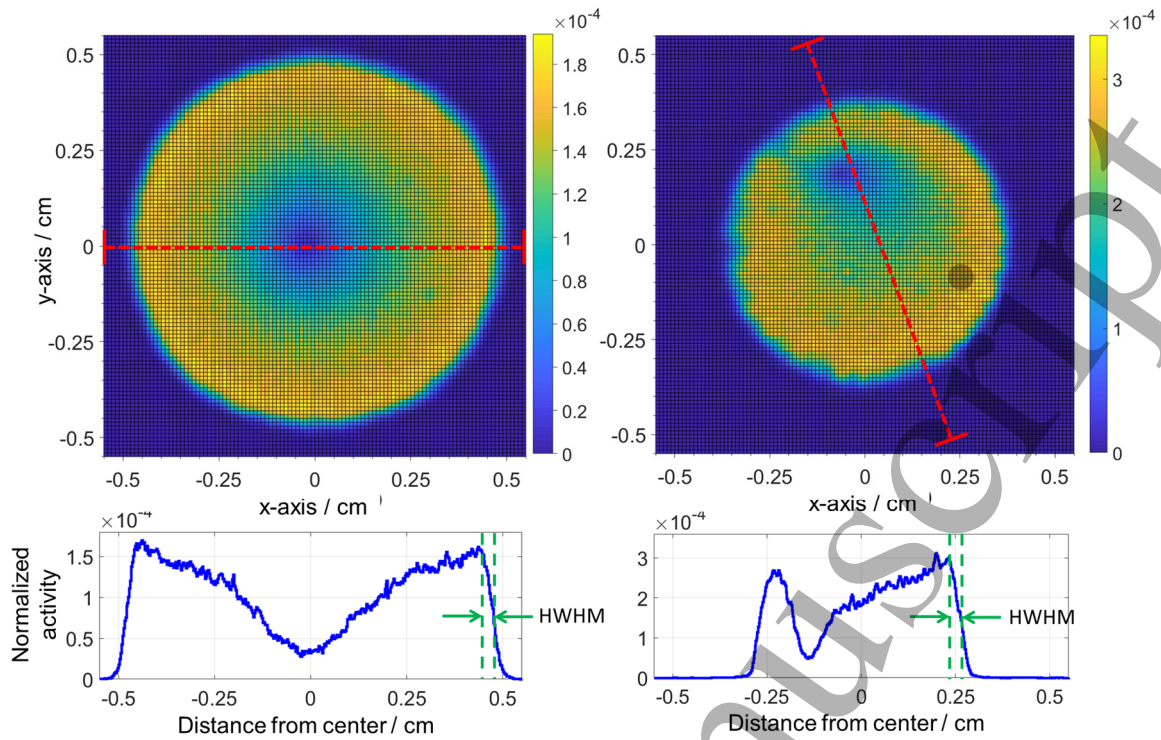


Figure 4. Left: activity distribution a_α of the α -particle source. Right: activity distribution a_X of the X-ray source. The two top panels show the surface normalized activity distribution per elementary surface of $100 \times 100 \mu\text{m}^2$ at the position (x, y) . The two bottom panels show 1-D activity distributions along the dashed lines. The arrows show the HWHM resolution of the profile.

For these reasons, two different sources of ^{241}Am with activities suited to the detector count rate were measured successively (table 1): an ^{241}Am source (called “X-ray source”) dedicated to the measurement of the X-ray rate n_{FEP} and an ^{241}Am source (called “ α -particle source”) with lower activity for the rate n_α ⁴. Therefore, two correction factors must be introduced in equation (4):

$$I(E) = \frac{N_{FEP}(E)}{N_\alpha} \cdot \frac{\Delta t_\alpha}{\Delta t_X} \cdot \frac{F_A \cdot F_{source} \cdot \varepsilon_{int,\alpha}}{\varepsilon_{int,X}(E) \times t_{Be}(E)} \quad (7)$$

where Δt_X and Δt_α are respectively the live times of the photon spectrum acquisition and the α -particle counting acquisition,

F_A is the ratio of the relative activities of the α -particle and the X-ray sources,

$\varepsilon_{int,X}(E)$ is the intrinsic efficiency for the X-rays with an energy E ,

$\varepsilon_{int,\alpha}$ is the intrinsic efficiency for the α -particles, lower than unity due to partial energy deposition in the absorber edges,

t_{Be} is the transmission of photons through the beryllium window, and F_{source} is a correction factor determined by MC simulations taking into account the differences between the geometries and the surface activity distributions of the sources.

3.2 The ^{241}Am source activities and the factor F_A

To determine the factor F_A , the activities of the two ^{241}Am sources were measured by DSA α -particle counting⁵[7]. The activity is given by the α -particle count rate divided by the geometrical efficiency of the DSA system; the latter has been calibrated by the characterization of the detection geometry dimensions.

Knowing that the activity factor F_A is the ratio between these activities determined with the same experimental system and the same spectrum processing technique, some of the uncertainty components are common, thus cancel each other. The activities of the α -particle source and the X-ray source are respectively 1816.4 (11) Bq and 32169 (34) Bq at the

⁴ It is not necessary to use an ^{241}Am source to measure n_α , another α -emitting radionuclide can be used since the measurement of n_α is equivalent to calibrating the geometrical efficiency.

⁵ Because F_A is the ratio between the two activities, an activity standardization is not necessary and a relative measurement of the source activities would have been sufficient.

measurement dates by the MMC (table 1). Only the uncertainties of the counting statistics, the extrapolation down to zero, the surface activity distribution and the reproducibility are considered. The activity distributions of the sources were measured by a source imager (figure 4). It results in $F_A = 0.05646$ (7).

3.3 Calculation of the correction factor F_{source}

The necessity to use two sources implies introducing the second correction factor F_{source} that takes into account the different geometrical efficiencies due to the different surface activity distributions (active diameters and inhomogeneity of the distributions) and the different source-collimator distances Z_{so-col} (table 1).

Given the detection geometry of the SMX3 set-up (figure 3), i.e. a large source diameter close to the collimator with a smaller hole diameter, the detection efficiency decreases with the source diameter. This dependence is amplified by the relatively large collimator thickness that acts as a double diaphragm for particles emitted at a distance from the center of the source larger than the radius of the collimator. Moreover, as shown in figure 4, the sources are inhomogeneous, so the count rate for a given source diameter will not only depend on the activity and the solid angle but also on the activity distribution of the source. To take into account the activity distributions, F_{source} can be expressed as:

$$F_{source} = \frac{\sum_{i=0}^{n-1} \sum_{j=0}^{n-1} a_{\alpha,ij}(x,y) \times f_{geo}(x,y,Z_{\alpha})}{\sum_{i=0}^{n-1} \sum_{j=0}^{n-1} a_{X,ij}(x,y) \times f_{geo}(x,y,Z_X)} \quad (8)$$

with,

$$S_{\alpha} = \sum_{i=0}^{n-1} \sum_{j=0}^{n-1} a_{\alpha,ij}(x,y) \times f_{geo,ij}(x,y,Z_{\alpha}) \quad (9)$$

$$S_X = \sum_{i=0}^{n-1} \sum_{j=0}^{n-1} a_{X,ij}(x,y) \times f_{geo,ij}(x,y,Z_X) \quad (10)$$

and where (x, y, z) is the position coordinate of an elementary surface with an area of $100 \times 100 \mu\text{m}^2$; the activity distribution has $n \times n$ elementary surfaces,

$f_{geo,ij}(x, y, z)$ is the geometrical efficiency for an elementary surface of $100 \times 100 \mu\text{m}^2$ at the position (x, y, z) ,

and $a_{X,ij}$ and $a_{\alpha,ij}$ are the normalized source activity distributions respectively for the α -particle and X-ray sources obtained from the source imager (figure 4), such that:

$$\sum_{X=0}^{n-1} \sum_{Y=0}^{n-1} a_{X,ij}(x,y) = \sum_{X=0}^{n-1} \sum_{Y=0}^{n-1} a_{\alpha,ij}(x,y) = 1 \quad (11)$$

The elementary geometrical efficiencies $f_{geo}(x, y, z)$ were calculated by MC simulations using the code PENELOPE. To model the detection geometry in the code, its dimensions involved in the solid angle were precisely determined using mainly two dimensional metrology systems: a Mitutoyo Quick vision measuring system for areas and a precision measuring column (Roch) for the distances and the thicknesses respectively. These dimensions are:

- the distances between the planes of the source disk, the collimator and the absorbers,
- the area of the collimator hole A_{col} ,
- the absorber area of the four pixels visible through the collimator A_{abs} .

The collimator aperture is smaller than the area formed by the four absorbers (figure 3), therefore, $A_{abs} = A_{col} - A_{gap}$, where A_{gap} is the gap area between the absorbers visible through the collimator. The total absorber area though the collimator aperture is $A_{abs} = 2.410$ (13) mm^2 , the collimator hole area is $A_{col} = 2.592$ (12) mm^2 and the gap area is $A_{gap} = 0.182$ (6) mm^2 , the absorber covering area is 93.1%. The collimator has a circular hole with a radius of $r_{col} = 0.9083$ (20) mm derived from its measured area. The area uncertainties are given by the uncertainty from the calibration of the vision measuring system and by the uncertainty for the detection of the surface edges by this system.

The distance between the plane of the source and the plane of the four absorbers facing the source is the sum of the three distances:

- 1- the distance between the plane of the rear of the collimator and the top plane of the absorbers $Z_{col-abs} = 0.491$ (37) mm. To have access to $Z_{col-abs}$, a lasermeter was used through the collimator hole,
- 2- the collimator thickness $e_{col} = 1.0066$ (28) mm,
- 3- the distance between the source plane and the plane of the collimator front side Z_{so-col} ,

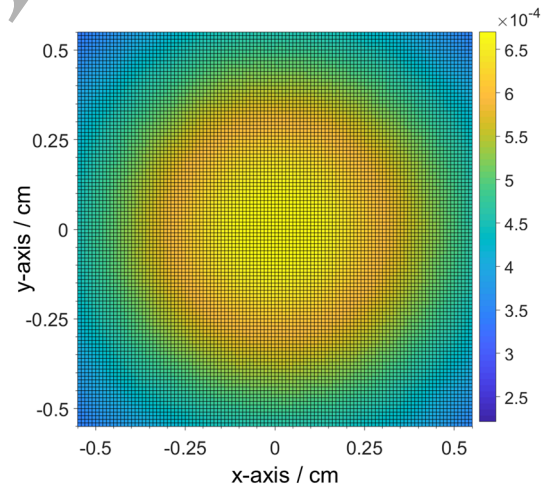


Figure 5. Geometrical efficiency $f_{geo}(x, y, Z_X)$ of the detector SMX3 obtained by MC simulations for each elementary area of $100 \times 100 \mu\text{m}^2$ at the positions (x, y, Z_X) .

All these dimensions of the detection geometry set-up were unchanged between the measurements of the two sources, except for the distance Z_{so-col} . The distance Z_{so-col} was modified by the different source backing made of stainless steel disks: Z_{so-col} is $Z_X = 16.339$ (8) mm and

$Z_\alpha = 15.845$ (12) mm respectively for the X -ray and the α -particle sources (table 1). Therefore, among the dimensions only Z_{so-col} contributes to the uncertainty of F_{source} .

The geometry modeled in the MC simulation is shown in figure 3. Figure 5 shows the simulated map of the geometrical efficiency $f_{geo}(x, y, z)$. One can notice that the geometrical efficiency varies significantly over the source area. It drops by 41% between the center and 5 mm from the center.

The uncertainty of the factor F_{source} was investigated through the uncertainties of the sums S_X and S_α (equations (9) and (10)). For each sum, several contributions were taken into account:

- the background in the source distribution images (figure 4),
- the position of the source center relative to the collimator center,
- the distance between the source and the collimator,
- the spatial resolution of the source distribution.

The background in the source activity distributions has very little impact on the sums, considering it will change the sums by less than 0.01%.

The spatial resolution is mainly due to the distance between the source and the radiographic film. The profile has a half-width at half maximum (HWHM) between 0.2 mm and 0.3 mm (figure 4). To estimate the effect of the spatial resolution, the sums S_α and S_X were calculated as a function of the HWHM for the simplified case of a homogenous source. Figure 6 shows that the values of the sums S_α and S_X decrease with the spatial resolution HWHM because a larger HWHM virtually spreads the activity outside the source where the f_{geo} efficiency decreases. This effect is cancelled for the most part, because F_{source} is the ratio between S_α and S_X . As seen in figure 6, F_{source} is slightly increased by a factor 1.00031 (7) due to the different source diameters.

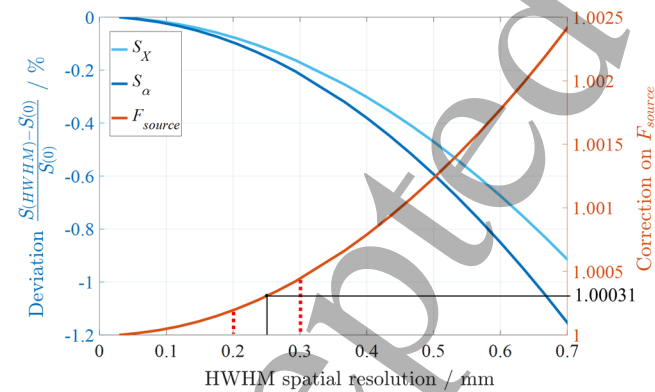


Figure 6. Left y-axis: deviations of the sums S_X and S_α from the sum of a source image with a zero HWHM spatial resolution. Right y-axis: correction on the factor $F_{source} = S_\alpha/S_X$. The dashed lines are the limits observed on the HWHM spatial resolution in figure 4.

The uncertainty of the eccentricity between the source centers and the z-axis is about 0.2 mm and the source orientations with

respect to the absorbers are unknown. These two uncertainties contribute 0.033% for both S_α and S_X . The uncertainties on the Z_α and Z_X distances contribute by 0.010% and 0.15% respectively for S_α and S_X . Nevertheless, in the factor F_{source} , the uncertainties of Z_α and Z_X are correlated, therefore, the factor F_{source} is 0.9783 (13) with an uncertainty dominated by the one of the difference between the source-collimator distances i.e. 0.494 (9) mm.

3.4 The intrinsic detection efficiencies

3.4.1 The intrinsic alpha efficiency $\epsilon_{int,\alpha}$. The absorbers are thick enough to fully absorb the α -particle energy but due to the detection geometry, some α -particles can reach the absorbers with an angle of up to 21° from the surface normal (figure 3); and hence some of α -particles can cross the absorber edges without depositing all their energy. In the spectrum, these events contribute to the background leading to a lower detection efficiency in the α -peaks. They could be taken into account by summing this background, however, other events contribute to the background, such as α -particles partially losing their energy in the collimator edges and interacting in the absorbers. Therefore, it was preferable to calculate the reduction in the intrinsic efficiency $\epsilon_{int,\alpha}$ by MC simulations using the code AlfaMC [27]. The simulated geometry takes into account the source diameter, the collimator and the four absorbers. In this case, absorbers are rectangular cuboids with perfectly sharp edges, but $\epsilon_{int,\alpha}$ depends on the sharpness of the edges, which is unknown. MC simulation gives an intrinsic efficiency of 0.9958; $\epsilon_{int,\alpha}$ lies between this latter value and unity (case of round edges), $\epsilon_{int,\alpha}$ and its uncertainty were calculated considering a uniform distribution between these two values: $\epsilon_{int,\alpha} = 0.9979$ (12).

3.4.2 The intrinsic photon efficiency, $\epsilon_{int,X}$. As shown in figure 2, although the intrinsic efficiency $\epsilon_{int,X}$ of photons between 5 keV and 25 keV is close to unity, there is about a 1% loss due to:

- the escape of photons or electrons from the top surface of the absorbers,
- the photons transmitted through the edge of the absorbers. Indeed, given the detection geometry, some photons arrive with an angle close to 19° from the normal of the absorber surface.

The intrinsic efficiency, $\epsilon_{int,X}$, was calculated by MC simulations and its uncertainty depends only on the interaction cross sections and on the transport of the photons and secondary electrons. The PENELOPE database of the attenuation coefficients relies on the data generated by the XCOM database and on the Dirac-Hartree-Fock-Slater model of Scofield [28–30]. For the photons, the uncertainties come from the cross sections, they are not well known and

depend strongly on the energy range and on the absorption edge energies [31]. Fortunately, Islam and co-workers precisely measured, in the energy range of interest, the attenuation coefficients of silver and gold, the materials composing our absorber [30, 31]. They observed a percentage difference of about 3% with the values from XCOM; this has been taken as a conservative relative uncertainty on the attenuation coefficients. For electrons, the uncertainty comes from their transport; since they are produced in a very large amount, the calculation of their transport has to distinguish between hard interactions (individually tracked) and soft interactions (statistical approximation calculation). The two types of calculation are set in the code PENELOPE by choosing cut-off energy parameters to get either precise or fast MC calculations.

To estimate these uncertainties, the intrinsic efficiency was simulated by varying many parameters:

- 1- the densities of gold and silver were changed by 3% to take into account the differences between measured and XCOM photon attenuation coefficients,
- 2- the cut-off values for the calculations of hard and soft interactions were changed to determine the impact of the more or less precise transport calculation of electrons,
- 3- the atomic numbers of the absorber materials were changed by ± 1 , keeping the same density of gold and silver in order to estimate the contribution of the cross section interactions as suggested in [34].

The results from all these MC simulations at 16 keV give an intrinsic detection efficiency of $\varepsilon_{int,X} = 0.9901$ (11). The intrinsic efficiency varying little between 11 keV and 25 keV, a constant relative uncertainty of 0.11% was considered for this energy range.

3.5 Transmission of the beryllium window

For the measurement of the X-ray spectrum, a 37.4 (23) μm thick beryllium window was used to absorb the α -particles and most of the electrons emitted during the decay of ^{241}Am .

The transmission of the beryllium window is shown in figure 2 and given by:

$$t_{Be} = e^{-\mu_{Be} m_{Be}/A_{Be}} \quad (12)$$

where μ_{Be} is the mass attenuation coefficient of beryllium, m_{Be} is the window mass, weighed with a microbalance, and A_{Be} is the area of the window determined with the vision measuring system.

The ratio m_{Be}/A_{Be} is 0.006681 (20) g/cm^2 .

The attenuation coefficient μ_{Be} is the dominant source of uncertainty for t_{Be} . Gerward measured and compared the

photoelectric cross sections of beryllium between 5 keV and 18 keV and noticed a deviation of the order of 5% from the data from the Dirac–Hartree–Fock–Slater model [35]. By taking this discrepancy as a conservative relative uncertainty on the mass attenuation coefficient, and by combining it with the uncertainty of the ratio m_{Be}/A_{Be} , a constant relative uncertainty of 0.03% was considered for the energy range 11 keV to 25 keV. The transmission at 16 keV is $t_{Be} = 0.99831$ (30).

4 The α -particle counting

The α -particle source of ^{241}Am was measured to determine the count rate such as:

$$n_{\alpha} = \sum_{i=1}^2 \sum_{j=1}^2 n_{\alpha,i,j} = \sum_{i=1}^2 \sum_{j=1}^2 N_{\alpha,i,j} / \Delta t_{\alpha,i} \quad (13)$$

where $N_{\alpha,i,j}$ are the numbers of α -particle counts in each pixel, the index i designates one of the two SQUID channels and the index j one of the two pixels of a given channel. The pixels of the same channel have the same live time $\Delta t_{\alpha,i}$.

The output voltages of the two SQUID channels were digitized and recorded continuously using a 16-bit resolution acquisition card at a sampling frequency of 100 kHz. The data were recorded during 9.6 days on a hard disk and the data analysis to obtain the spectrum was performed and optimized offline.

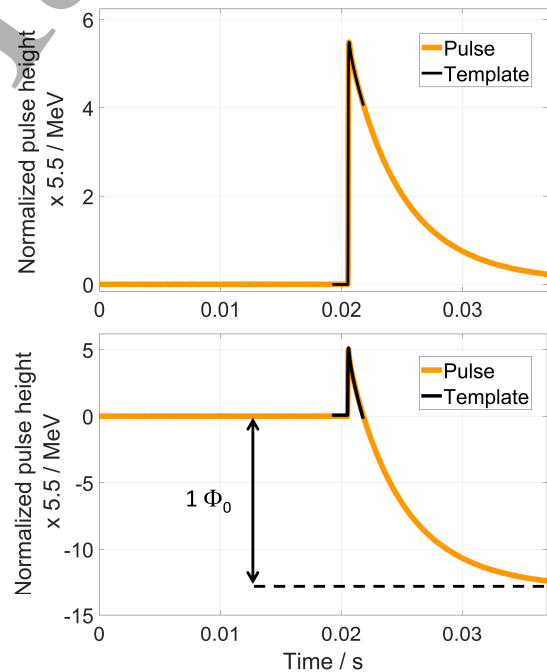


Figure 7. Pulses of 5.5 MeV α -particles and their truncated pulse template scaled by least squares fitting. Top, a regular pulse. Bottom, a pulse with a flux jump of $1 \Phi_0$.

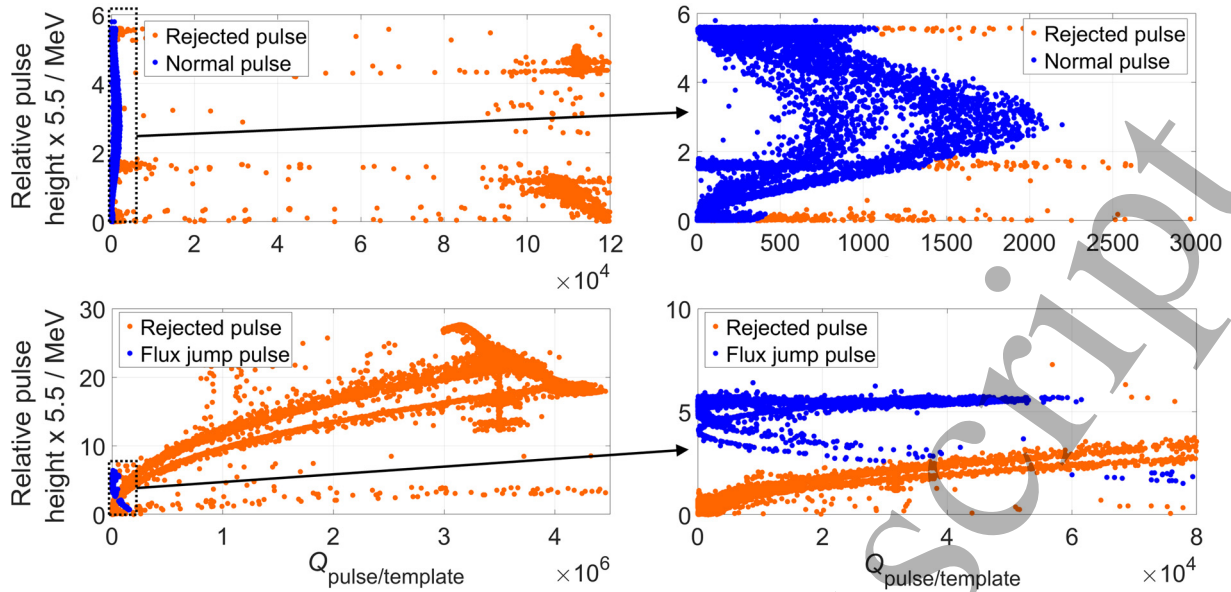


Figure 8. Pulse heights as a function of the pulse shape parameter $Q_{\text{pulse/template}}$ obtained after the least squares fit with the truncated templates. The two top subplots present the results using the regular pulse template (figure 7). The two bottom subplots show the results using the template of flux jump pulses. The two right subplots are a zoom around the selected pulses.

As explained in section 3.1, the SMX3 detector is too sensitive for measuring α -particle energies when it is in its normal operating conditions; its sensitivity was reduced by choosing a smaller permanent current I_0 in the pick-up coils, lower than 1 mA. However, one channel showed too high sensitivity for which some pulses had a flux jump⁶ of $1 \Phi_0^3$ (figure 7). These flux jumps are due to detected α -particles and have to be taken into account in the count rate n_α .

Each channel shows positive and negative pulses according to which of the two absorbers has absorbed a particle. Once the off-line trigger has detected the pulses in the continuous streams, the pulse heights are determined by scaling the height of a truncated pulse template of $W = 2.56$ ms on each triggered pulse with a least squares fit (figure 7). This pulse height analysis degrades the energy resolution by about 20% compared with an optimal filtering analysis, but it has the advantage to strongly reduce the pile-up probability and the dead time; indeed optimal filtering requires longer templates, typically about 16 ms [36]. More details of the data processing are given in [37].

For the channel having some flux jumps, two pulse templates were applied: one template representative of regular pulses and the other one representative of the flux jump pulses (figure 7). Each of the two types of pulses can easily be selected by comparing the pulse shape parameter $Q_{\text{pulse/template}}$ calculated as the mean squared error of the fits between the pulses and the two templates (figure 8).

⁶ A flux jump occurs when the variation of flux in the SQUID is faster than the maximum slew rate of the SQUID electronics, the working point of the SQUID imposed by the feedback reaction becomes unstable and the SQUID may

The live times $\Delta t_{\alpha,j}$ were determined by two methods. The first method applies an extendable dead time. However, with this method, the live time must be corrected by the pile-up rejection. Indeed, when a pulse is triggered, a second pulse can arrive within the time window W required to estimate the pulse energy (figure 7); the resulting pulse energy is not properly determined and can be out of the region of interest in the energy spectrum, leading to a missing count. These pulse pile-ups were rejected based on a selection criterion of the parameter $Q_{\text{pulse/template}}$. However, regarding the live time, these pile-ups are valid pulses and hence the live time must be corrected by the probability P_0 of not having a pulse during the time W :

$$P_0 = \exp\left(-\frac{\tau_r \cdot W}{2}\right) \quad (14)$$

where τ_r is the count rate of each channel, Given the recorded count rates, P_0 was calculated to be 99.73% and 99.65% respectively for the two channels with a truncated template.

The second method is the pulser method. It consists in adding pulses in the continuously digitized raw stream data with a unique height and with random times of arrival. The rate of the pulser pulses n_p being known, the live time Δt_α is given by the count number N_p in the pulser peak of the spectrum divided by n_p . The main advantage is that the determination of the live time is independent of pile-up

jump to another working point. This appears on the electronics output as a voltage jump equivalent to an integer number of Φ_0 .

rejection. However, a large pulser count is required to reach a small statistical uncertainty, which tends to increase also the dead time. By comparing the results of the two methods, we can ensure that no potentially hidden dead time is missed, in particular from saturations.

The count numbers $N_{\alpha,i,j}$ were determined by summing all the counts in a region of interest (ROI) between 4.0 MeV and 5.6 MeV in order to take into account: most of the counts in the left tail due to the straggling of α -particles in the source and all the α -emissions of ^{241}Am lying between 4.76 MeV and 5.54 MeV (figure 9). A nearly constant background is present between 1 MeV and 4 MeV with a level much higher than the one in the DSA α -particle spectrum obtained in section 3.2. Part of this background is due to straggling in the source and must be taken into account in N_{α} . While from the DSA spectrum the source straggling is expected to be 0.1 count per keV around 3 MeV, the observed level is 1.1 counts per keV. We attributed the excess of background to scattering of α -particles in the detector surrounding and to straggling in the edges of the collimator and the absorbers, the detection set-up being not configured to minimize these effects. Therefore, the count number $N_{\alpha,i,j}$ was subtracted of the background by an extrapolation from the range 1 MeV - 4 MeV to 4 MeV - 5.6 MeV. The total alpha rate n_{α} is 1.0408 (14) counts per second, with a relative uncertainty dominated by the counting statistics (relative contribution of 0.13%).

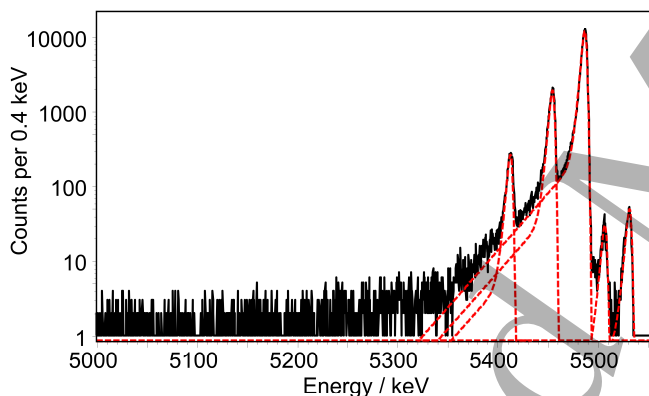


Figure 9. The spectrum of α -particles obtained with the MMC SMX3. The FWHM instrumental resolution is about 3.3 keV. The dashed lines represent the fit of the five main peaks.

5. L X-ray spectrum of ^{237}Np from the decay of ^{241}Am

5.1 Signal and data processing

The X-ray source of ^{241}Am was measured during 15 days at 13 mK, the SQUID electronics output voltage, digitized with a resolution of 16-bits and a sampling frequency of 500 kHz, was recorded continuously on a hard disk.

Here, two methods were applied to determine the pulse heights. The first one determines them by fitting a truncated pulse template to the detected pulses with a time window $W = 2.05$ ms. This method was preferable for the determination of the $L\alpha$, $L\eta\beta$, and $L\gamma$ group PEIs and the total

PEI: although it is not the best pulse height estimator, it minimizes the pile-up probability and therefore gives a more reliable live time with lower uncertainty. The second method estimates the pulse energy after applying an optimal filter [36]; it gives the best amplitude estimation and the best energy resolution (15% better than with the truncated template method) to separate as many lines as possible. However, this optimal filtering required a long pulse time window $W = 16.4$ ms with a larger pile-up probability of 5.8% versus 0.73% with the truncated template method. This method was preferred to determine the PEIs of the individual LX-ray transitions; they were renormalized with respect to the total PEI obtained from the first truncated template method. The live time was determined after applying an extendable dead time, and it was checked using the pulser method as described in section 4.

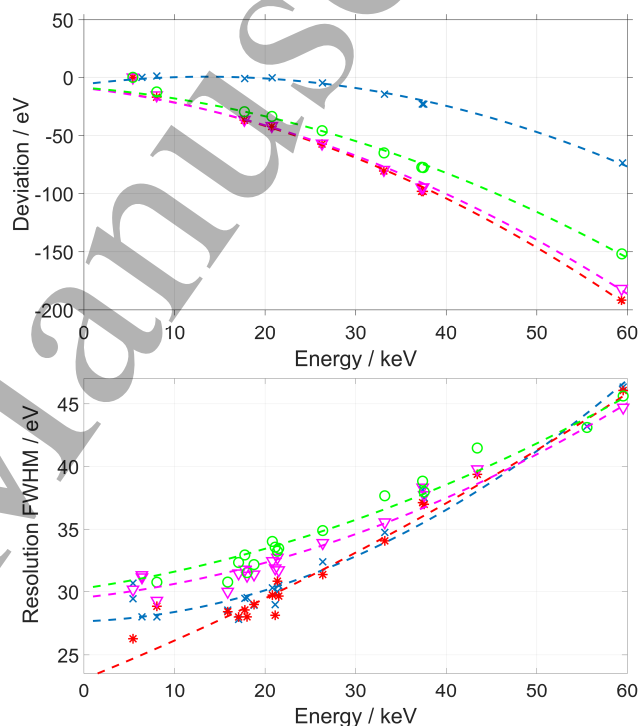


Figure 10. Top, non-linearities of each pixel given by the difference between the measured energies and the tabulated energies. Bottom, energy resolution of each pixel. Each marker type represents the experimental data of one pixel. The lines correspond to the fit of the experimental data with a 2nd order polynomial.

Each pixel provides a spectrum with its own energy resolution and energy non-linearity which are slightly different from each other. In order to obtain a total energy spectrum by summing the individual spectra without degrading the energy resolution nor distorting the energy peak shape, the energy scales² were linearized and their energy resolutions were homogenized to match the poorest resolution among the four spectra [37]. For each pixel, the deviation from the linear response was determined as the difference between

a number of measured energies and their corresponding tabulated data from [38]. The deviation was fitted with a second order polynomial to allow the non-linearity to be corrected (figure 10). Afterward, the individual corrected spectra were summed after being weighted by their respective live times (equation (13)).

5.2 Spectrum processing of L X-rays.

In order to extract the count rate in the FEP, n_{FEP} , the L X-ray spectrum was processed with the software Colegram in a ROI between 10.4 keV and 24.5 keV and around 4.8 keV to determine the PEI of the L_1 - L_3 transition [39]. Due to the high statistical precision (6×10^6 counts) and the energy resolution (between 28.0 eV and 33.8 eV FWHM), the spectrum is highly detailed and many lines and structures have to be taken into account during the spectrum processing (figures 11 and 12):

- the X-ray diagram lines of Np correspond to X-ray transitions occurring when the atoms are singly ionized; the corresponding peaks were fitted with a single Voigt function, i.e. the convolution of a Lorentzian function and a Gaussian function. The Lorentzian function represents the natural line width of the transition given by the sum of the initial and the final atomic level widths. The Gaussian function is the contribution from the detector energy resolution. For the most intense and well-separated lines, one of the two widths is a free parameter, while for the other lines the two widths are fixed. The Lorentzian fixed widths were set according to the values from [40,41]. The fixed Gaussian widths were set according to the least good energy resolution among the four pixels (figure 10)⁷. The energies and the heights of the Voigt functions are free parameters.

- the satellite X-ray structures come from X-ray transitions of multiply ionized atoms: these structures are present for the L_3 X-rays. Indeed most of the L_3 vacancies are created following a Coster-Kronig transition with an initial vacancy in L_2 or L_1 . The resulting atom is multi-ionized with at least two vacancies, one in L_3 and a second vacancy (spectator vacancy) in an outer shell. When the L_3 vacancy is filled by an outer electron, the emitted X-rays have a higher energy than that of the diagram transition, due to the different electronic configurations. X-ray satellites have a complex shape due to the tens of possible transitions, depending on the quantum numbers of the electronic configuration [42]. The shape cannot be fitted with a single Voigt; instead, each satellite structure was fitted using two or three Voigt functions with the same width as the diagram lines, and with free energies and free heights (figure 11).

- the background between 10.4 keV and 24.5 keV was fitted with a constant function and three step functions. The constant function represents the Compton background from the γ -rays. The three step functions represent the background produced by the main L X-ray groups: $L\alpha$, $L\beta$ and $L\gamma$. The step functions are centered on each group energy (figure 12).

- the left tailed components appearing on the left side of each main X-ray peak were fitted with exponential functions (figure 12). The origin of these tails is not clear; they are also present on the γ -ray peaks of 26.3 keV and 59.5 keV. While for X-rays, left tails could come from physical processes of the atomic rearrangement, such as radiative Auger emission (RAE) [43,44], the γ -ray line profile is expected to be emitted with a perfect Lorentzian shape with a very narrow natural line width. Therefore, left tails must be caused either by Compton scattering of photons in the surrounding materials between the source and the absorber, e.g. the beryllium window, or by a detector response distortion [12]. The contribution from Compton scattering has been excluded by MC simulations, the response distortion is therefore assumed to be responsible for these tails. The hypothesis to explain this distortion is that many 59.5 keV γ -rays pass through the absorbers and interact in the MMC chip nearby the sensor leading to a strong change in the temperature of the chip. Therefore, thermodynamic quantities of materials thermally coupled with the MMC are modified, affecting the pulse shape and the measured energy.

In figure 13, the γ -ray peaks are well fitted with a Gaussian and two exponential functions representing a short and a long tail. The area of the long component is constant with the energy and represents 0.5% of the peak area while the area of the short exponential components decreases from 2.0% to 1.3% at 59.5 keV and 26.3 keV, respectively. In the L X-ray spectrum, the long exponential components are clearly present with the same ratio tail area over peak area for γ -rays as well as for the most intense L X-rays, i.e. $\sim 0.5\%$; this component was fitted for the most intense L X-ray peaks (figure 12). Concerning the short left tail components, they are hardly noticeable for L X-rays due to the complexity of the spectrum and due to the shape of the Voigt functions. Thus, the short components were ignored assuming that they are included in the Voigt functions. Indeed, figure 13 shows that for a Gaussian and a Voigt with equal area, a Voigt function strongly overlaps with the tails, in contrast with the Gaussian function. Moreover, for the most intense peaks, one of the two widths (Gaussian or Lorentzian) is a free parameter in order to include the short tails in the Voigt.

⁷ For the main X-ray lines, the Lorentzian width could have been a free parameter, however the shape of a Lorentzian function has extended « wings » compared to the Gaussian

shape, so the wings tend to alter the peaks depending on certain background features and increase the peak area.

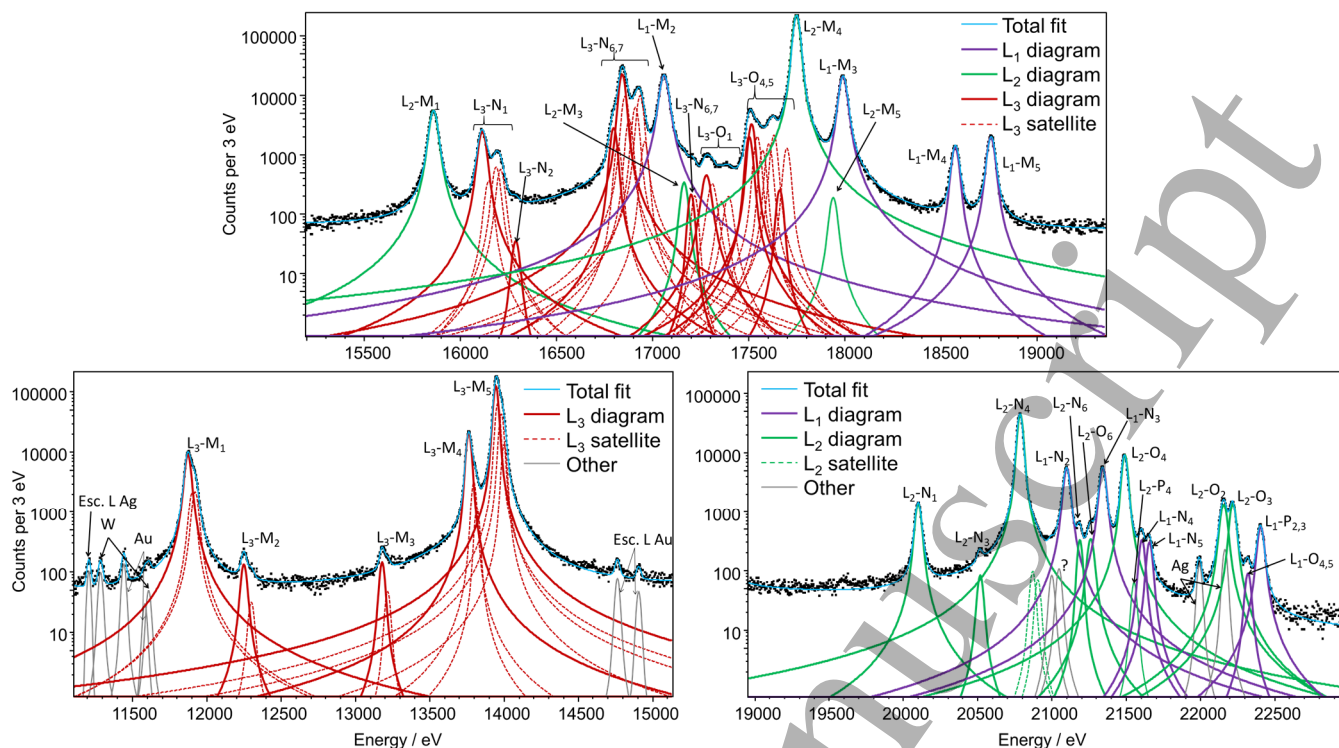


Figure 11. Detailed spectrum processing of the L X-ray peaks in three energy ranges: L_1 - $L\alpha$, $L\eta\beta$ and $L\gamma$. The solid lines are the diagram transitions and the dashed lines are the satellites. The other Voigt functions are fluorescence and escape peaks. Left tail components are shown in figure 12 for clarity.

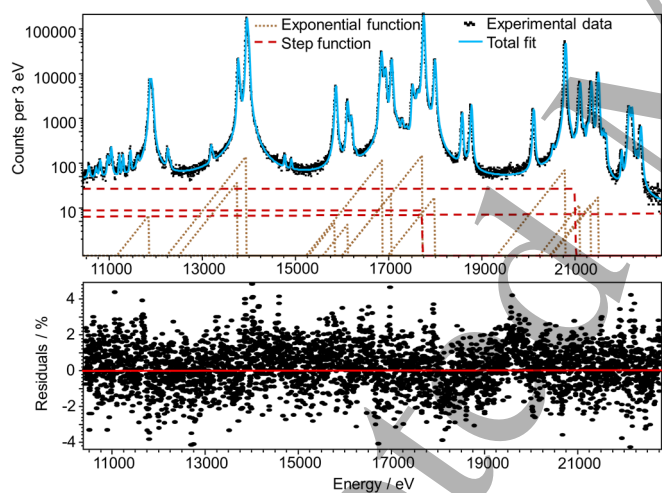


Figure 12. Top, experimental L X-ray energy spectrum and its total fit. The step functions fit the background and the exponential functions fit the long left tails of the main peaks. The fit of the individual peaks is detailed in figure 11 for more clarity. Bottom, resulting residuals between the fit and the experimental data.

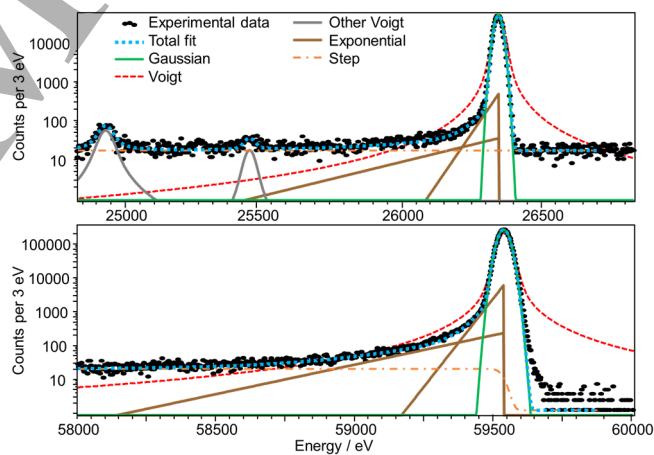


Figure 13. Spectrum processing of the γ -ray peaks at 26.3 keV (top) and 59.5 keV (bottom) and their left tails. The γ -ray FEPs are fitted with one Gaussian function and two exponential functions for the left tails. The step function fits the background. The dashed Voigt function has the same area as the Gaussian.

After applying this fitting procedure, the residuals between the fit and the experimental spectrum did not show any particular trend adjacent to the peaks (figure 12). There are only a few lines interfering in the ROI coming from the fluorescence of gold, silver and tungsten; they are easily distinguished in the spectrum (figure 11).

6. L X-ray emission intensities of ^{237}Np from the decay of ^{241}Am

6.1 Emission intensities of the Siegbahn L X-ray groups

For the following Siegbahn lines and groups, $L\iota$, $L\varsigma$, $L\tau$, $L\alpha$, $L\eta$, $L\beta$ and $L\gamma$, the absolute PEIs were determined with equation (7), the rate n_{FEP} of each group being the sum of the rates in the Voigt functions (diagram lines and satellite structures) and the exponential functions in the respective energy range. The present absolute total L X-ray emission, i.e. the sum of these group intensities, is 37.90 (12) per 100 decays⁸. Figure 14 shows the comparison of the present value with the published data and with the recommended value from Chechev [21]. A good agreement with all the data is observed and the present uncertainty is about a factor 2 lower than the most precise previous measurement (table 2).

Table 2 and figure 15 show and compare the absolute PEIs of $L\iota$, $L\alpha$, $L\eta\beta$ and $L\gamma$, obtained in this work and the ones published in the literature from various measurements with semiconductor detectors. The present PEIs are in good agreement with the published data, with uncertainties about two times lower than the best measurements [18,45].

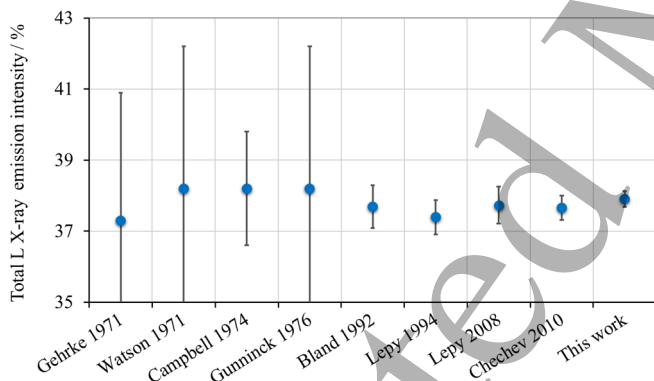


Figure 14. Total absolute emission intensities referenced in [21] and the result of the present work. The uncertainty bars are plotted for a coverage factor $k = 2$.

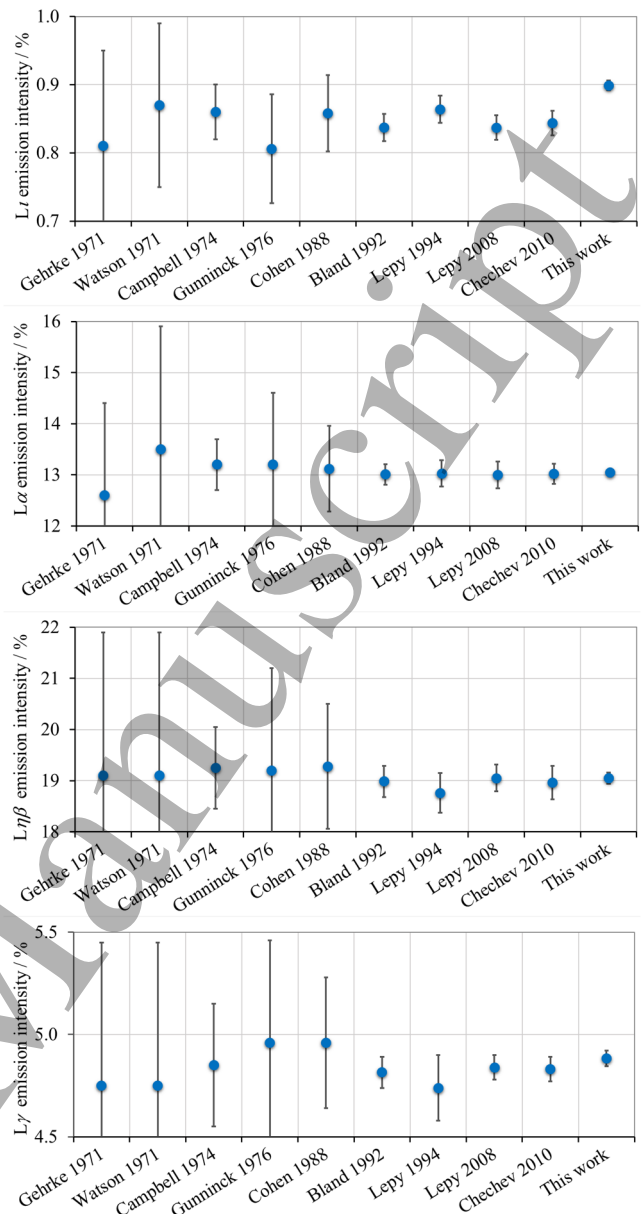


Figure 15. Absolute emission intensities of the groups $L\iota$, $L\alpha$, $L\eta\beta$ and $L\gamma$, referenced in [21] and the results from the present work. The uncertainty bars are plotted for a coverage factor $k = 2$.

The only intensity group which is not consistent with the recommended value and with most of the measurements is the $L\iota$ intensity, while all the published values agree. Theoretical calculations do not seem to support our value, the deviation $D(\iota/\alpha)$ between the theoretical intensity ratio $L\iota/L\alpha$ and the present results is $D(\iota/\alpha) = 9.2\%$, while the data in the literature are in agreement with the theoretical emission rate ratio of $L\iota/L\alpha$ [46,47]. Nevertheless, nothing can explain such

⁸ The X-ray line L_{1-3} presented in table 3 is not included in the total L X-ray emission intensity in order to be comparable with published data.

a discrepancy in the present experiment; the efficiency cannot vary by about 9% within a few keV while there is no possible edge discontinuity; in addition, the $L\iota$ and $L\alpha$ peaks are well separated, allowing for a safe spectrum processing, and no other peaks from fluorescence or from escape photons can overlap with $L\iota$.

In a past measurement with MMCs, a discrepancy was also observed for the $L\iota/L\alpha$ ratio of Bi X-rays emitted from the decay of ^{210}Pb ($D(\iota/\alpha) = 16.4\%$) while we observed a good agreement with the calculated ratio of U X-rays emitted by the decay of ^{238}Pu $L\iota/L\alpha$ ($D(\iota/\alpha) = 1.2\%$) [37,48]. In fact, the ratio $L\iota/L\alpha$ depends strongly on the satellite intensity of the L_3 transitions. Indeed, the observable satellites represent a few tens of percent of the L_3 transition intensity for ^{210}Pb and ^{241}Am , while it is only a few percent for ^{238}Pu ⁹. For ^{210}Pb and ^{241}Am , respectively 99% and 61% of L_3 vacancies are produced consecutively to Coster-Kronig transitions from L_1 and L_2 vacancies, versus only 15% for ^{238}Pu . After the Coster-Kronig transition, the spectator vacancies are mostly located in M_4 or M_5 subshells, the creation of an M_1 vacancy being energetically not possible. Therefore the decay channel of an $M_{4,5}$ electron filling the L_3 (i.e. an $L\alpha$ transition) vacancy is reduced in favor of the L_3 - M_1 ($L\iota$ transition) because there is one electron missing in the $M_{4,5}$ subshells [49,50]. Finally, the disagreement with the calculated $L\iota/L\alpha$ ratio is not surprising because calculated data assume single vacancy states [46]. Thus, we are confident in the present measurement of the $L\iota$ intensity even if we cannot explain why the other measurements have lower $L\iota$ PEIs.

6.2 Emission intensities of L X-ray transitions

Owing to the excellent resolution of the MMC SMX3 and the large counting statistics, it was possible to measure the intensities of 32 L X-rays of ^{237}Np from the decay of ^{241}Am in the energy range 10.4 keV - 24.5 keV, and the L_1 - L_3 PEI at 4.8 keV⁸.

For each L X-ray transition, its PEI is the sum of the diagram line, with the satellites structure and left tail component when they are present. Table 3 shows the results of PEI for the 33 X-ray transitions. Some closely spaced transitions cannot be well separated, these transitions are either X-ray satellites (see L_3 - $N_{4,5}$, L_3 - $N_{6,7}$, L_3 - $O_{4,5}$ in figure 11) that spread over several tens of eV and/or X-rays involving electrons from outer shells with closely spaced binding energies (L_3 - $O_{1,2,3}$, L_3 - $P_{1,4,5}$, L_1 - $O_{4,5}$ in figure 11). In these cases, the PEIs are the sum of the overlapped transitions.

While the spectrum processing had little impact on the uncertainty of the Siegbahn groups (table 3), some PEIs vary

greatly depending on the fitting procedure applied, especially the X-rays sitting on the left tail of an intense peak, for example for L_3 - M_3 , L_2 - N_3 or L_3 - $O_{4,5}$. Often simply ignored, systematic errors related to the fitting procedure are difficult to estimate. In the present work, the systematic errors were calculated from different results derived of different assumptions (how the left tail areas are shared between the peak areas) and different procedures (with and without left tails). The partial relative uncertainties for each transition are detailed in table 3.

6.3 Uncertainty budget

The uncertainties involved in equation (7) to measure the PEIs, and detailed throughout the article, are summarized in table 4. One can distinguish three types of uncertainty:

- the counting statistics uncertainties, which appears in the correction factor F_A , the count numbers N_α and N_{FEP} , they contribute with a relative uncertainty of 0.17%,
- the uncertainty of the corrections related to the interaction of particles (intrinsic efficiencies $\varepsilon_{int,\alpha}$ and $\varepsilon_{int,X}$, beryllium window transmission t_{Be}) with a relative contribution of 0.20%,
- the uncertainty related to the geometry (source positioning, and source activity inhomogeneities) with a relative contribution of 0.18%.

The weights of these contributions are comparable and, together, they represent 93% of the total combined uncertainty. For future measurements, it is interesting to see how these contributions could be reduced. The counting uncertainty could be reduced to 0.1% whilst maintaining reasonable measurement times.

The geometry uncertainty can be reduced to 0.06% with more appropriate source holder and source geometries. It remains much more challenging to reduce the uncertainty on the intrinsic efficiencies. For now, it is not clear how to reduce the uncertainty of the photon intrinsic efficiency, $\varepsilon_{int,X}$. Potentially, the uncertainty of the α -particle intrinsic efficiency, $\varepsilon_{int,\alpha}$, could be suppressed by using a non-pixelated absorber to get rid of the pixel edge effects. However, this will obviously be at the detriment of the resolution and the count rate capabilities. Taking into account all these reductions, a total relative uncertainty closer to 0.2% could be achieved.

⁹ Satellites are observable only if their energy shift is significantly higher than the width of the diagram peaks and the resolution of the detectors. For L_3 -M transitions, it is the

case when the spectator vacancy is in an M subshell: the shift is in the order of a few tens of eV, while when the spectator vacancy is in an N shell the shift is the order of a few eV.

7. Conclusion

Measurements have been made of the total L X-ray emission intensity of ^{237}Np , from the decay of ^{241}Am , with a relative uncertainty of 0.32%, and details of 33 L X-ray emission intensities by combining the method inspired by Lépy and co-workers with the performances of a metallic magnetic calorimeter. The emission intensities were determined by measuring the ratio between the L X-ray rate and the α -particle emissions rate from two ^{241}Am sources with the same detection system. These measurements are deemed accurate assuming the intrinsic detection efficiency of the photons is close to 100%.

It has been proved that, with the current detection system, photon emission intensities of other α -emitting radionuclides from a few keV to 25 keV could be measured with the same level of uncertainty. Thus, the obtained emission intensities are free of any efficiency calibration from other emission intensities and free of standard sources established by other primary methods. This makes the present results truly *absolute* emission intensities.

Acknowledgements

This work was performed as part of the EMPIR Project 17FUN02 MetroMMC. This project has received funding from the EMPIR program co-financed by the Participating States and from the European Union's Horizon 2020 research and innovation program.

Table 2. Comparison between the L X-ray emission intensities of ^{237}Np from 100 decays of ^{241}Am for some Siegbahn groups and lines obtained in this work with those measured or evaluated in the literature. The references of the measured data are cited in [21]. The combined uncertainties are given for one standard deviation.

Line or group	Gehrke and Lokken 1971	Watson and Li 1971	Campbell and McNelles 1974	Gunninck et al. 1976	Cohen* 1988	Bland et al. 1992	Lépy et al. [45] 1994	Lépy et al. [18] 2008	Chechev and Kuzmenko** [21] 2009	This work
$L\iota$	0.81 (7)	0.87 (6)	0.86 (2)	0.806 (40)	0.858 (28)	0.837 (10)	0.864 (12)	0.837 (9)	0.844 (9)	0.8989 (38)
$L\varsigma$	-	-	-	-	0.017 (5)	0.0073 (13)	-	-	-	0.01024 (26)
$L\tau$	-	-	-	-	0.0302 (37)	0.032 (10)	-	-	-	0.0101 (8)
$L\alpha$	12.6 (9)	13.5 (12)	13.20 (25)	13.2 (7)	13.12 (42)	13.01 (10)	13.03 (13)	13.00 (12)	13.02 (10)	13.046 (41)
$L\eta$	19.1 (14)	19.1 (14)	19.25 (40)	19.2 (10)	0.380 (12)	0.377 (15)	0.369 (12)	0.404 (5)	0.384 (20)	0.3745 (23)
$L\beta$					18.9 (6)	18.61 (15)	18.39 (19)	18.65 (13)	18.58 (13)	18.68 (6)
$L\gamma$	4.75 (35)	4.75 (35)	4.85 (15)	4.96 (25)	4.96 (16)	4.815 (38)	4.74 (8)	4.84 (3)	4.83 (3)	4.883 (20)
Total	37.3 (18)	38.2 (20)	38.2 (8)	38.2 (2.0)	38.2 (12)	37.69 (30)	37.39 (24)	37.73 (26)	37.66 (17)	37.90 (12)

*relative measurement normalized to the $L\alpha$ intensity from this work.

**evaluated data

Accepted Manuscript

Table 3. Photon emission intensities of L X-rays emitted by ^{237}Np from the decay of ^{241}Am per 100 decays. The two last columns show the two partial relative uncertainties from the counting statistics and fitting procedure; a third contribution related to the detection efficiencies is 0.33% (not shown) equal for all the transitions. The uncertainties are given for one standard deviation.

X-ray transition		Energy (eV)	PEI per 100 decays	Relative uncertainties			Siegbahn group	PEI per 100 decays	Relative uncertainties		
UIPAC	Siegbahn			Total	Fitting procedure	Counting statistics			Total	Fitting procedure	Counting statistics
L ₁ -L ₃	-	4820	0.2289 (15)	0.65%	0.41%	0.42%					
L ₃ -M ₁	L ₁	11873	0.8989 (38)	0.42%	0.13%	0.21%					
L ₃ -M ₂	L _t	12250	0.01024 (26)	2.57%	0.64%	1.96%					
L ₃ -M ₃	L _s	13179	0.0101 (8)	7.59%	7.33%	1.98%					
L ₃ -M ₄	L α_1	13762	1.2581 (49)	0.39%	0.19%	0.18%					
L ₃ -M ₅	L α_2	13944	11.788 (38)	0.32%	0.13%	0.06%	L α	13.046 (41)	0.31%	0.084%	0.069%
L ₂ -M ₁	L η	15862	0.3745 (23)	0.60%	0.29%	0.33%					
L ₃ -N ₁	-	16113	0.2389 (14)	0.59%	0.32%	0.41%					
L ₃ -N _{4,5}	L $\beta_{2,15}$	16796 - 16958	2.912 (14)	0.48%	0.36%	0.12%					
L ₁ -M ₂	L β_4	17061	1.602 (5)	0.33%	0.04%	0.16%					
L ₃ -N _{6,7}	L β_7'	17207 - 17222	0.01636 (49)	2.99%	2.54%	1.55%					
L ₃ -O _{1,2,3}	L β_7	17275 - 17357	0.0818 (32)	3.95%	3.88%	0.69%					
L ₃ -O _{4,5} - L ₃ -P _{1,4,5}	L β_5	17501 - 17630	0.638 (9)	1.45%	1.39%	0.25%	L β	18.68 (6)	0.31%	0.064%	0.058%
L ₂ -M ₄	L β_1	17750	11.665 (39)	0.34%	0.16%	0.06%					
L ₂ -M ₅	-	17938	0.00976 (31)	3.21%	2.49%	2.01%					
L ₁ -M ₃	L β_3	17992	1.3242 (49)	0.37%	0.14%	0.17%					
L ₁ -M ₄	L β_{10}	18577	0.0756 (6)	0.82%	0.25%	0.72%					
L ₁ -M ₅	L β_9	18762	0.1150 (8)	0.69%	0.21%	0.59%					
L ₂ -N ₁	L γ_5	20101	0.1037 (10)	0.93%	0.63%	0.62%					
L ₂ -N ₃	-	20516	0.0056 (9)	16.41%	16.19%	2.65%					
L ₂ -N ₄	L γ_1	20785	2.916 (12)	0.41%	0.20%	0.12%					
L ₁ -N ₂	L γ_2	21098	0.4330 (20)	0.46%	0.19%	0.30%					
L ₂ -N ₆	L γ_8'	21186	0.01811 (31)	1.72%	0.83%	1.48%					
L ₂ -O ₁	L γ_8	21260	0.02841 (48)	1.69%	1.17%	1.18%					
L ₁ -N ₃	L γ_3	21341	0.4363 (20)	0.46%	0.20%	0.30%					
L ₂ -O ₄	L γ_6	21489	0.6260 (30)	0.48%	0.28%	0.25%	L γ	4.883 (20)	0.41%	0.26%	0.11%
L ₂ -P ₁	-	21555	0.00386 (16)	4.02%	2.41%	3.20%					
L ₂ -P ₄	-	21595	0.02246 (31)	1.39%	0.28%	1.33%					
L ₁ -N ₅	-	21656	0.02041 (30)	1.46%	0.32%	1.39%					
L ₁ -O ₂	L γ_4'	22155	0.1139 (8)	0.67%	0.15%	0.59%					
L ₁ -O ₃	L γ_4	22216	0.1057 (7)	0.70%	0.15%	0.61%					
L ₁ -O _{4,5}		22319	0.00639 (16)	2.58%	0.61%	2.49%					
L ₁ -P _{2,3}		22404	0.04361 (46)	1.05%	0.34%	0.95%					

Table 4. Uncertainty budget of all the quantities used to determine the photon emission intensities from equation (7).

PEI I	>0.32%	n_{α}	0.14%	N_{α}	0.13%	Counting statistics	0.13%		
				Background extrapolation	0.020%				
				Δt_{α}	0.056%	Clock	0.050%		
						Pile-up rejection	0.019%		
				n_{FEP}^*	>0.12%	N_{FEP}^*	>0.084%	Counting statistics*	>0.058%
						Spectrum processing*	>0.061%		
		F_A	0.12%	X -ray source activity	0.11%	Counting	0.10%		
						Source geometry and positioning	0.030%		
				α -particle source activity	0.061%	Counting	0.053%		
						Source geometry and positioning	0.030%		
				F_{source}	0.17%			Eccentricity and orientation	0.033%
								Disk thicknesses	0.17%
		Source image	<0.01%						
Intrinsic efficiencies	0.16%			$\epsilon_{int,\alpha}$	0.12%				
				$\epsilon_{int,X}$	0.11%				
t_{Be}	0.03%			Attenuation coefficients of Be	0.030%				
				Weight and area of Be window	<0.01%				

*The most favorable case has been chosen for the relative uncertainties of $L\beta$ emission intensity.

References

- [1] Debertin K and Helmer R G 1988 *Gamma- and x-ray spectrometry with semiconductor detectors* (Amsterdam ; New York : New York, NY, USA: North-Holland ; Sole distributors for the USA and Canada, Elsevier Science Pub. Co)
- [2] Bé M-M and Chechev V P 2013 Recommended standards for gamma ray intensities *Nucl. Instrum. Methods Phys. Res. Sect. Accel. Spectrometers Detect. Assoc. Equip.* **728** 157–72
- [3] Herman M, Nichols A L and International Atomic Energy Agency 2007 *Update of X ray and gamma ray decay data standards for detector calibration and other applications* (Vienna, Austria: International Atomic Energy Agency)
- [4] Campbell J L and McGhee P L 1986 State-of-the-art efficiency determination for a Si(Li) X-ray detector in the 3–40 keV energy range *Nucl. Instrum. Methods Phys. Res. Sect. Accel. Spectrometers Detect. Assoc. Equip.* **248** 393–404
- [5] Lépy M-C, Brondeau L, Ménesguen Y, Pierre S and Riffaud J 2018 Consistency of photon emission intensities for efficiency calibration of gamma-ray spectrometers in the energy range from 20 keV to 80 keV *Appl. Radiat. Isot.* **134** 131–6
- [6] Pommé S 2015 Typical uncertainties in alpha-particle spectrometry *Metrologia* **52** S146–55
- [7] Pommé S 2015 The uncertainty of counting at a defined solid angle *Metrologia* **52** S73–85
- [8] W. Bambynek 1967 Precise solid-angle counting Proc. Int. Symp. on Standardization of Radionuclides (Vienna: International Atomic Energy Agency)
- [9] Denecke B 1987 Measurement of the 59.5-keV gamma-ray emission probability in the decay of ^{241}Am with a $4\pi\text{-CsI(Tl)}$ - sandwich spectrometer *Int. J. Rad. Appl. Instrum. [A]* **38** 823–30
- [10] Elvira V H, Peyrés V, Roteta M, Fernández-Sotillo A and García-Toraño E 2020 Absolute determination of low-energy X-ray emission rates with a proportional counter *Appl. Radiat. Isot.* **160** 109113
- [11] Martin L J and Burns P A 1992 The HPGe as a defined-solid-angle detector for low-energy photons *Nucl. Instrum. Methods Phys. Res. Sect. Accel. Spectrometers Detect. Assoc. Equip.* **312** 146–51
- [12] Van Gysel M, Lemberge P and Van Espen P 2003 Description of Compton peaks in energy-dispersive x-ray fluorescence spectra *X-Ray Spectrom.* **32** 139–47
- [13] Plagnard J, Hamon C and Lépy M C 2008 Study of scattering effects in low-energy gamma-ray spectrometry *Appl. Radiat. Isot.* **66** 769–73
- [14] Boson J, Ågren G and Johansson L 2008 A detailed investigation of HPGe detector response for improved Monte Carlo efficiency calculations *Nucl. Instrum. Methods Phys. Res. Sect. Accel. Spectrometers Detect. Assoc. Equip.* **587** 304–14
- [15] Elanique A, Marzocchi O, Leone D, Hegenbart L, Breustedt B and Oufni L 2012 Dead layer thickness characterization of an HPGe detector by measurements and Monte Carlo simulations *Appl. Radiat. Isot.* **70** 538–42
- [16] Vidmar T and Likar A 2002 Automated construction of detector models for efficiency interpolation in gamma-ray spectrometry *Appl. Radiat. Isot.* **56** 99–103
- [17] Helmer R G, Hardy J C, Iacob V E, Sanchez-Vega M, Neilson R G and Nelson J 2003 The use of Monte Carlo calculations in the determination of a Ge detector efficiency curve *Nucl. Instrum. Methods Phys. Res. Sect. Accel. Spectrometers Detect. Assoc. Equip.* **511** 360–81
- [18] Lépy M C, Plagnard J and Ferreux L 2008 Measurement of ^{241}Am L X-ray emission probabilities *Appl. Radiat. Isot.* **66** 715–21

- [19] Rodrigues M, Mariam R and Loidl M 2017 A metallic magnetic calorimeter dedicated to the spectrometry of L X-rays emitted by actinides ed A Plompen, F-J Hamsch, P Schillebeeckx, W Mondelaers, J Heyse, S Kopecky, P Siegler and S Oberstedt *EPJ Web Conf.* **146** 10012
- [20] Fleischmann A, Enss C and Seidel G M 2005 Metallic Magnetic Calorimeters *Cryogenic Particle Detection* vol 99, ed C Enss (Berlin, Heidelberg: Springer Berlin Heidelberg) pp 151–216
- [21] Chechev V P and Kuzmenko N K 2010 Decay data evaluation project (DDEP): Updated evaluations of the ²³³Th and ²⁴¹Am decay characteristics *Appl. Radiat. Isot.* **68** 1578–82
- [22] Kempf S, Fleischmann A, Gastaldo L and Enss C 2018 Physics and Applications of Metallic Magnetic Calorimeters *J. Low Temp. Phys.* **193** 365–79
- [23] Boyd S T P, Kim G-B, Hall J A, Cantor R H and Friedrich S 2020 Metallic Magnetic Calorimeters for High-Accuracy Nuclear Decay Data *J. Low Temp. Phys.* **199** 681–7
- [24] Burck A, Kempf S, Schäfer S, Rotzinger H, Rodrigues M, Wolf T, Gastaldo L, Fleischmann A and Enss C 2008 Microstructured Magnetic Calorimeter with Meander-Shaped Pickup Coil *J. Low Temp. Phys.* **151** 337–44
- [25] Nuclear Energy Agency 2019 *PENELOPE 2018: A code system for Monte Carlo simulation of electron and photon transport: Workshop Proceedings, Barcelona, Spain, 28 January – 1 February 2019* (OECD)
- [26] Rodrigues M, Loidl M and Le-Bret C 2012 A Novel Type of Absorber Presenting a Constant Detection Efficiency for up to 25 keV X-Ray Photons *J. Low Temp. Phys.* **167** 510–5
- [27] Peralta L and Louro A 2014 AlfaMC: A fast alpha particle transport Monte Carlo code *Nucl. Instrum. Methods Phys. Res. Sect. Accel. Spectrometers Detect. Assoc. Equip.* **737** 163–9
- [28] Sabbatucci L and Salvat F 2016 Theory and calculation of the atomic photoeffect *Radiat. Phys. Chem.* **121** 122–40
- [29] Seltzer S 1987 XCOM-Photon Cross Sections Database, NIST Standard Reference Database 8
- [30] Scofield J H 1973 *Theoretical photoionization cross sections from 1 to 1500 keV*. (United States)
- [31] Chantler C T 1995 Theoretical Form Factor, Attenuation, and Scattering Tabulation for $Z=1-92$ from $E=1-10$ eV to $E=0.4-1.0$ MeV *J. Phys. Chem. Ref. Data* **24** 71–643
- [32] Islam M T, Rae N A, Glover J L, Barnea Z, de Jonge M D, Tran C Q, Wang J and Chantler C T 2010 Measurement of the x-ray mass attenuation coefficients of gold in the 38 – 50 - keV energy range *Phys. Rev. A* **81** 022903
- [33] Islam M T, Tantau L J, Rae N A, Barnea Z, Tran C Q and Chantler C T 2014 Measurement of the X-ray mass attenuation coefficients of silver in the 5–20 keV range *J. Synchrotron Radiat.* **21** 413–23
- [34] Bochud F O, Laedermann J-P and Sima O 2015 Uncertainty associated with Monte Carlo radiation transport in radionuclide metrology *Metrologia* **52** S191–9
- [35] Gerward L 1992 Theoretical upper and lower limits to experimental X-ray attenuation coefficients *Nucl. Instrum. Methods Phys. Res. Sect. B Beam Interact. Mater. At.* **69** 407–12
- [36] Szymkowiak A E, Kelley R L, Moseley S H and Stahle C K 1993 Signal processing for microcalorimeters *J. Low Temp. Phys.* **93** 281–5
- [37] Mariam R, Rodrigues M, Loidl M, Pierre S and Lourenço V 2022 Determination of L-X ray absolute emission intensities of ²³⁸Pu, ²⁴⁴Cm, ²³⁷Np and ²³³Pa radionuclides using a metallic magnetic calorimeter *Spectrochim. Acta Part B At. Spectrosc.* **187** 106331
- [38] Deslattes R D, Kessler E G, Indelicato P, de Billy L, Lindroth E and Anton J 2003 X-ray transition

- energies: new approach to a comprehensive evaluation *Rev. Mod. Phys.* **75** 35–99
- [39] Ménesguen Y and Lépy M-C 2021 COLEGRAM, a flexible user-friendly software for processing of ionizing radiation spectra *Nucl. Instrum. Methods Phys. Res. Sect. Accel. Spectrometers Detect. Assoc. Equip.* **1003** 165341
- [40] Hoszowska J, Dousse J-Cl and Rhème Ch 1994 Linewidths of photoinduced L x rays of uranium *Phys. Rev. A* **50** 123–31
- [41] Campbell J L and Papp T 2001 WIDTHS OF THE ATOMIC K–N7 LEVELS *At. Data Nucl. Data Tables* **77** 1–56
- [42] Parente F, Chen M H, Crasemann B and Mark H 1981 L x-ray satellite energies *At. Data Nucl. Data Tables* **26** 383–466
- [43] Åberg T 1971 Theory of the Radiative Auger Effect *Phys. Rev. A* **4** 1735–40
- [44] Campbell J L, Perujo A, Teesdale W J and Millman B M 1986 $K\alpha$, $K\beta$, and radiative Auger photon intensities in K x-ray spectra from atoms in the $20 \leq Z \leq 40$ region *Phys. Rev. A* **33** 2410–7
- [45] Lépy M C, Duchemin B and Morel J 1994 Comparison of experimental and theoretical L X — ray emission probabilities of ^{241}Am , ^{239}Pu and ^{240}Pu *Nucl. Instrum. Methods Phys. Res. Sect. Accel. Spectrometers Detect. Assoc. Equip.* **353** 10–5
- [46] Scofield J H 1974 Hartree-Fock values of L x-ray emission rates *Phys. Rev. A* **10** 1507–10
- [47] Campbell J L and Wang J-X 1989 Interpolated Dirac-Fock values of L-subshell x-ray emission rates including overlap and exchange effects *At. Data Nucl. Data Tables* **43** 281–91
- [48] Rodrigues M, Cassette P, Lépy M-C, Loidl M and Ménesguen Y 2016 Determination of absolute photon emission intensities of ^{210}Pb *Appl. Radiat. Isot.* **109** 500–6
- [49] Larkins F P 1971 Dependence of fluorescence yield on atomic configuration *J. Phys. B At. Mol. Phys.* **4** L29–32
- [50] Campbell J L 2003 Measurement of the L1 sub-shell fluorescence and Coster–Kronig yields of bismuth *J. Phys. B At. Mol. Opt. Phys.* **36** 3219–31